Diagnosing Radial Ventilation in Dropsonde Observations of Hurricane Sam (2021)

BRIAN H. TANG,[a] ROSIMAR RIOS-BERRIOS,[b] AND JUN A. ZHANG[c]

[a] *Department of Atmospheric and Environmental Sciences, University at Albany, State University of New York, Albany, New York*
[b] *National Center for Atmospheric Research, Boulder, Colorado*
[c] *NOAA/AOML/Hurricane Research Division, University of Miami/CIMAS, Miami, Florida*

(Manuscript received 3 October 2023, in final form 23 April 2024, accepted 7 May 2024)

ABSTRACT: This study presents a method to diagnose radial ventilation, the horizontal flux of relatively low-θ_e air into tropical cyclones, from dropsonde observations. We used this method to investigate ventilation changes over three consecutive sampling periods in Hurricane Sam (2021), which underwent substantial intensity changes over 3 days. During the first and last periods, coinciding with intensification, the ventilation was relatively small due to a lack of spatial correlation between radial flow and θ_e azimuthal asymmetries. During the second period, coinciding with weakening, the ventilation was relatively large. The increased ventilation was caused by greater shear associated with an upper-level trough, tilting the vortex, along with dry, low-θ_e air wrapping in upshear. The spatial correlation of the radial inflow and anomalously low-θ_e air resulted in large ventilation at mid- to upper levels. Additionally, at low to midlevels, there was evidence of mesoscale inflow of low-θ_e air in the stationary band complex. The location of these radial ventilation pathways and their effects on Sam's intensity are consistent with previous idealized and real-case modeling studies. More generally, this method offers a way to monitor ventilation changes in tropical cyclones, particularly when there is full-troposphere sampling around and within a tropical cyclone's core.

SIGNIFICANCE STATEMENT: Ventilation, the injection of relatively dry and/or cool air into a tropical cyclone, may weaken a storm. In contrast, the lack of ventilation is favorable for intensification. The purpose of this study is to present a method to diagnose ventilation using aircraft dropsonde observations. Using dropsonde observations collected in Hurricane Sam (2021), there was a period of increased lateral ventilation in two regions around the storm that coincided with when the storm rapidly weakened. The results suggest that monitoring ventilation from dropsonde observations, when available, may be useful for anticipating ventilation-induced intensity changes in tropical cyclones and further studying ventilation pathways.

KEYWORDS: Dry intrusions; Hurricanes/typhoons; Wind shear; Tropical cyclones; Dropsondes

1. Introduction

Environmental vertical wind shear and ventilation, the intrusion of low-equivalent potential temperature θ_e air into a tropical cyclone (TC), is an important environmental constraint on tropical cyclones (Emanuel et al. 2004; Tang and Emanuel 2010; Riemer et al. 2010, 2013; Alland et al. 2021a,b; Alland and Davis 2022). Tropical cyclones tend to develop and intensify when ventilation is limited and weaken when ventilation is substantial (Tang and Emanuel 2012a; Chavas 2017; Lin et al. 2017).

There are two types of ventilation pathways: downdraft ventilation and radial ventilation. Downdraft ventilation is the flushing of low-θ_e air into the boundary layer by evaporatively driven downdrafts in both deep convection and stratiform precipitation (Powell 1990; Riemer et al. 2010, 2013; Zhang et al. 2013; Alland et al. 2021a; Wadler et al. 2021; Yu et al. 2023a). Radial ventilation is the horizontal transport of low-θ_e air from the near environment into the inner core, where it dilutes the high-θ_e inner core and is entrained into buoyant updrafts (Simpson and Riehl 1958; Cram et al. 2007; Tang and Emanuel 2010, 2012b; Gu et al. 2015; Alland et al. 2021b; Fischer et al. 2023). The inner core is roughly the innermost 100 km around the low-level center of a tropical cyclone, encompassing the eye, eyewall, and inner rainbands (Weatherford and Gray 1988; Houze 2010). In addition to the import of relatively low-θ_e air, the export of relatively high-θ_e air may weaken the radial θ_e gradient near the radius of maximum wind and reduce the intensity (Gu et al. 2015). In this study, we will focus on diagnosing radial ventilation and its structure.

Radial ventilation may be induced by the vortex tilt, the storm-relative flow, and/or midlevel inflow in rainbands (Riemer and Montgomery 2011; Davis and Ahijevych 2012; Didlake and Houze 2013; Alland et al. 2021b). First, vertical wind shear tilts the TC vortex, oftentimes resulting in a stable tilt orientation in the downshear-left direction (Jones 1995; Reasor et al. 2004, 2013; Reasor and Montgomery 2015; Fischer et al. 2022). The misaligned vortex produces wavenumber-1 asymmetries in the radial flow that are of opposite sign at upper and lower levels (Zhang et al. 2013; DeHart et al. 2014; Boehm and Bell 2021). For example, for a downshear-left tilt direction, there is anomalous inflow upshear and anomalous outflow downshear at upper levels. Such a wavenumber-1 asymmetry in the radial flow may import low-θ_e air into the TC. Second, the storm-relative flow, associated with the vertically sheared environmental flow, also has a wavenumber-1 projection onto the radial flow above and

Corresponding author: Brian H. Tang, btang@albany.edu

DOI: 10.1175/MWR-D-23-0224.1

below the steering level. Third, shear acts to organize rainband convection (e.g., Corbosiero and Molinari 2002; Hence and Houze 2012) and the stationary band complex (Riemer 2016). Mesoscale descending inflow, found in the stratiform portion of these shear-organized rainbands, may import low-θ_e air inward (Didlake and Houze 2013; Alland et al. 2021a).

The vertical structure of radial ventilation also varies across TCs. Tang and Emanuel (2012b) hypothesized that radial ventilation in the middle troposphere (around 600 hPa) near the climatological θ_e minimum would be most detrimental to a TC. The import of low-θ_e air from around this level by mesoscale descending inflow in rainbands would potentially tap into this large θ_e deficit. Recent studies (Fu et al. 2019; Ryglicki et al. 2019; Finocchio and Rios-Berrios 2021; Alland and Davis 2022; Fischer et al. 2023; Shi and Chen 2023) have found that radial ventilation above that level and below the outflow (around 300–600 hPa) is also important, as a result of radial inflow pathways despite smaller θ_e deficits higher up in the troposphere. The spatial distribution of θ_e or relative humidity around the TC also affects the ventilation structure, especially upshear (Zawislak et al. 2016; Rios-Berrios and Torn 2017; Alvey et al. 2020; Richardson et al. 2022). Here, we seek to further explore the vertical structure of radial ventilation pathways.

Ventilation may be viewed from both Lagrangian and Eulerian perspectives. In Lagrangian perspectives, trajectories are examined in model simulations of sheared TCs to study the transport of low-θ_e air and mixing with high-θ_e air within the TC. Lagrangian approaches are useful for quantifying how ventilation directly affects convection and the secondary circulation (Cram et al. 2007; Riemer and Laliberté 2015; Euler et al. 2019; Yu et al. 2023a). Eulerian perspectives quantify ventilation as an eddy flux of θ_e. For example, radial ventilation may be quantified as $u'\theta_e'$, where u is the storm-relative radial wind (Tang and Emanuel 2010). The primes denote perturbations from the azimuthal mean in a cylindrical coordinate system moving with the low-level center. Eulerian approaches are useful for visualizing the structure of ventilation pathways and quantifying ventilation magnitude at a system scale (Alland et al. 2021a,b). Given the reliance on observations in this study, our methods to diagnose ventilation will be motivated by Eulerian approaches.

Diagnosing ventilation directly from observations is challenging, as it requires observations of both the wind and thermodynamic variables in and around a system, preferably over the full troposphere. As a proxy, Tang and Emanuel (2012a) devised a ventilation index that is assumed to scale with the actual ventilation. The ventilation index has been primarily used to model and understand bulk TC genesis and intensity behaviors (Lin et al. 2017; Hoogewind et al. 2020; Hsieh et al. 2020). In contrast, here, we demonstrate a way to diagnose ventilation via dropsonde observations, which may be useful for monitoring and anticipating ventilation-induced intensity changes in individual TCs.

The goals of this study are to 1) devise a framework to diagnose radial ventilation from dropsonde observations, 2) apply this framework to investigate radial ventilation in Hurricane Sam (2021), and 3) link radial ventilation structures to aspects of the intensity change and structure of Sam. Section 2 gives an overview of Hurricane Sam and the environmental evolution during the time period of interest. Section 3 describes the diagnostic radial ventilation framework. Section 4 presents the radial ventilation in Sam. Section 5 offers a way to calculate a summary ventilation metric, and section 6 ends with conclusions.

2. Hurricane Sam

a. Storm evolution

Hurricane Sam traversed over open waters of the central part of the North Atlantic from 22 September to 5 October 2021. The period of interest in our study is from 25 to 28 September 2021. Figure 1 shows a summary of Sam's satellite and intensity evolution during this time period, which was characterized by rapid changes. Satellite snapshots were created from the NCEP/CPC Merged Infrared dataset (Janowiak et al. 2017). Sam rapidly intensified during the first 24 h of the period, developing a symmetric and compact inner core. Sam reached peak intensity [135 kt (1 kt $\approx$ 0.51 m s^{-1})] at 1800 UTC 26 September 2021. There was a rapid deterioration of the satellite presentation over the next 24 h, with the eye disappearing and the deep convection becoming asymmetric. During this period, Sam's intensity decreased by 30 kt, satisfying the criterion for overwater rapid weakening (Wood and Ritchie 2015). On 28 September 2021, Sam's inner core became better organized and the storm reintensified by 10 kt.

While not the focus of our study, an eyewall replacement cycle commenced at the start of the rapid weakening period (Pasch and Roberts 2022). A larger eyewall reestablished itself on 28 September 2021, associated with the reorganization of the inner core.

b. Environment

Figure 2 shows the main mid- to upper-level features of interest interacting with Hurricane Sam, as depicted in the ERA5 reanalysis (Hersbach et al. 2020). At 0000 UTC 26 September 2021, there was an upper-level trough, given by the area of larger 200-hPa potential vorticity (PV) to the west of Sam in Fig. 2a. Additionally, dry air at 300–500 hPa was present to the north of the system. The 850–200-hPa wind shear, however, was only 1.7 m s^{-1}, and this low shear was conducive for Sam's rapid intensification (Fig. 1).

At 0000 UTC 27 September 2021 (Fig. 2b), the TC moist envelope became more asymmetric, with the dry air wrapping around the west side of the system and getting closer to the TC center. Additionally, the southwesterly shear increased, peaking at 5.5 m s^{-1} at 0600 UTC 27 September 2021 (Fig. 1). The increase in shear was due to Sam approaching the upper-level trough, seen by the area of >0.5 PVU (1 PVU = 10^{-6} K kg^{-1} m^2 s^{-1}) impinging on the circulation, which imparted a stronger southerly upper-level flow on the TC. The combination of the increasing shear and the dry-air intrusion indicated the likely presence of ventilation due to an unfavorable trough interaction (Leroux et al. 2016; Peirano et al. 2016).

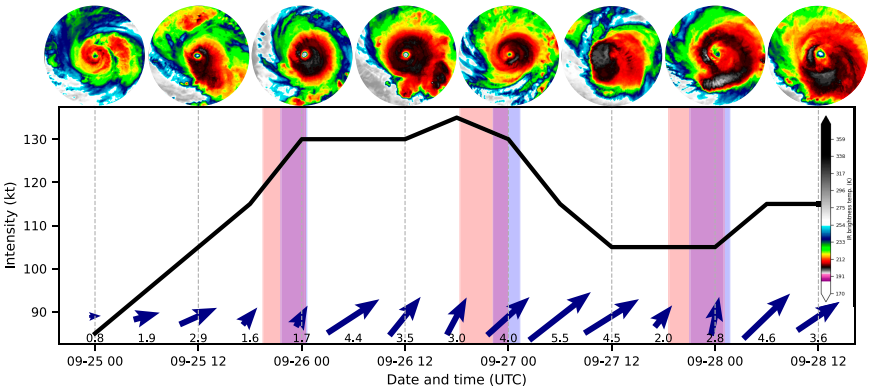

FIG. 1. Intensity time series of Hurricane Sam from 0000 UTC 25 Sep 2021 to 1200 UTC 28 Sep 2021. Shaded regions correspond to dropsonde sampling periods for the G-IV (red), P-3 (blue), and both aircraft (purple). Snapshots of infrared satellite imagery, centered on the storm over a 2° radius disk, are shown in 12-h increments along the top of the figure. The 850–200-hPa shear vector and magnitude (m s^{-1}), from the Statistical Hurricane Intensity Prediction Scheme developmental database, are shown in 6-h increments along the bottom of the figure.

As quickly as the shear increased, it abated in the subsequent 12 h and was variable thereafter. While dry air and the deformed trough still remained in the vicinity of Sam, the moist envelope became more symmetric (Fig. 2c).

c. *Dropsonde sampling*

Sam represents a good observational case because of three consecutive days of sampling by both G-IV and P-3 aircraft during overlapping time periods (Figs. 1 and 3), as part of the joint NOAA Hurricane Field Program and ONR Tropical Cyclone Rapid Intensification initiative, providing an augmented number of dropsonde observations. Additionally, as shown in Fig. 3, the flight patterns were consistent day-to-day with the G-IV conducting circumnavigation patterns around the storm and the P-3 conducting rotated (figure-4) patterns through the storm. As will be shown, this consistency and coverage of observations are advantageous for examining radial ventilation changes.

3. Methods

a. *Dropsonde processing*

Dropsonde data were obtained from NOAA and quality controlled using the Atmospheric Sounding Processing Environment software (Martin and Suhr 2021). The G-IV dropsondes typically sample from about 200 hPa to the surface, and the P-3 dropsondes typically sample from about 700 hPa to the surface, so there were more observations taken in the lower troposphere.

For each of the three sampling periods (Fig. 3), the dropsonde observations were transformed into a cylindrical grid in a storm-relative frame of reference. First, the storm motion was subtracted from the horizontal wind to obtain the storm-relative winds. The storm motion was calculated from the 2-min TC position estimates from NOAA. Observation locations were determined relative to the time-interpolated TC position. Second, the transformation of scalar and vector variables into a cylindrical grid followed the methods of Ahern and Cowan

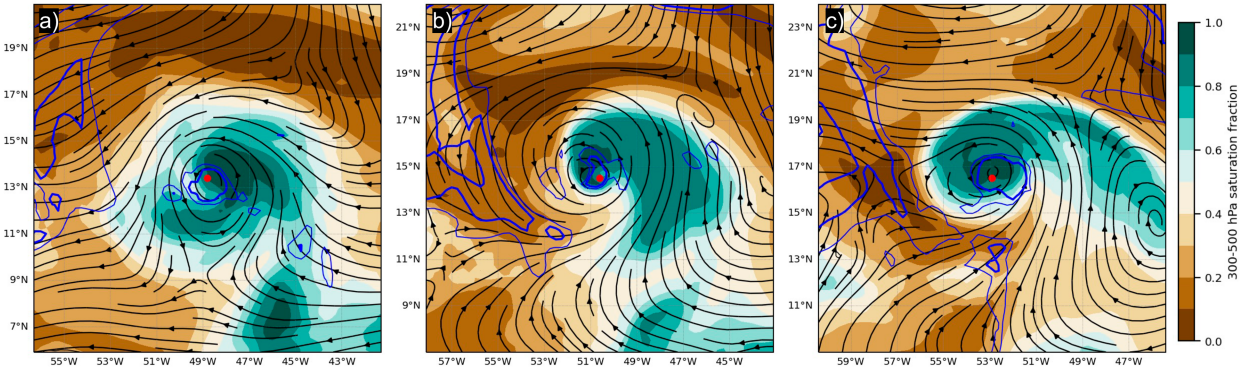

FIG. 2. The 300–500-hPa saturation fraction (shading) and layer-average winds (streamlines), along with a 200-hPa potential vorticity (0.5 PVU thin, blue contour and 1 PVU thick, blue contour) at (a) 0000 UTC 26 Sep 2021, (b) 0000 UTC 27 Sep 2021, and (c) 0000 UTC 28 Sep 2021. The red dot indicates the best track location of Sam at each time.

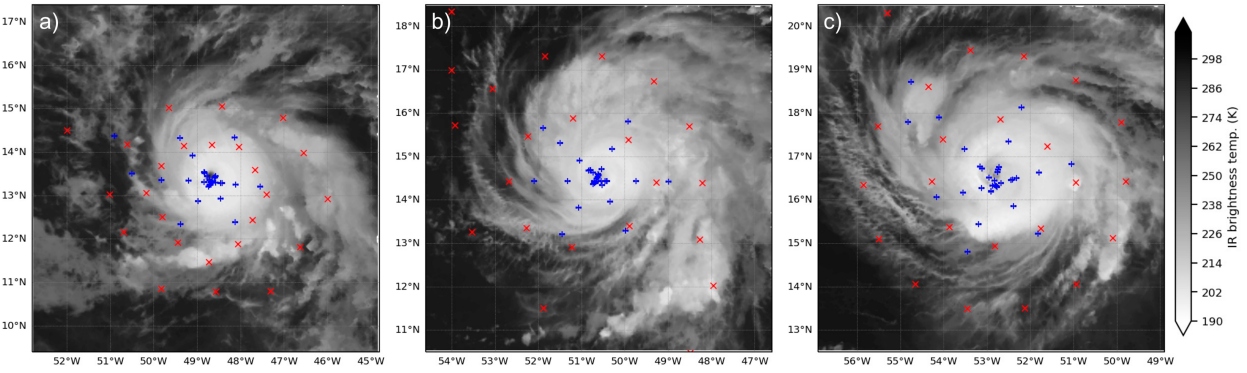

FIG. 3. Dropsonde launch locations for the sampling periods around (a) 0000 UTC 26 Sep 2021, (b) 0000 UTC 27 Sep 2021, and (c) 0000 UTC 28 Sep 2021. G-IV drop locations are given by the red ×'s, and P-3 drop locations are given by the blue +'s. The infrared satellite image at 0000 UTC on each day is also shown.

(2018). In doing so, we assumed that the observations collected over the sampling period could be analyzed as if they were collected instantaneously. This assumption was necessary to gain azimuthal coverage for the radial ventilation calculation, described next.

b. *Radial ventilation calculation*

Radial ventilation was quantified using the eddy flux of θ_e as follows:

$$u'\theta_e'.$$

The calculation required an estimate of the azimuthal mean of u and θ_e in order to calculate the perturbations. To estimate the azimuthal mean, we constructed a 150-km-wide, 10-hPa-deep annulus centered on *each* observation. Then, all observations within this annulus were retained, excluding inner-core observations within 1.5 times the radius of maximum wind. We tested different annulus widths, and a 150-km width was a good compromise between retaining a sufficient number of observations without encompassing too large of an area. The inner-core mask was needed due to large radial gradients in the inner-core u and θ_e that produced excessively large perturbation values. An initial check was done to ensure there were dropsonde data in all four quadrants around the annulus. Provided this check was passed, observations were binned by quadrant and averaged. Then, the four quadrants were averaged to yield an azimuthal average. This method reduced bias in the azimuthal average due to inhomogeneous sampling. Once an azimuthal average was obtained, the perturbation quantities were calculated to diagnose the radial ventilation. The calculation preserved the vertical resolution of the dropsonde data.

4. Results

a. *Horizontal structure*

Figure 4 shows the components of the ventilation calculation for the first sampling period around the end of Sam's rapid intensification. The calculation is split into three layers: 300–500, 500–700, and 700–900 hPa, which we will refer to as the upper, middle, and lower layers. In each layer, there was a general wavenumber-1 pattern in u' (Figs. 4a,d,g); however, there were less coherent asymmetries in θ_e' (Figs. 4b,e,h). As a result, the radial ventilation in each layer was generally weak and disorganized (Figs. 4c,f,i). The ventilation magnitude was predominately <5 m s^{-1} K with a few isolated outliers. Sam's rapid intensification was consistent with a lack of ventilation, which could otherwise constrain intensification.

Figure 5 shows a similar ventilation analysis for the second sampling period around the start of rapid weakening. In contrast to the first sampling period, there were distinct wavenumber-1 asymmetries in both u' and θ_e'. The shear was southwesterly, and the tilt was toward the north-northwest. We will discuss the role of the tilt later in the manuscript. In the upper layer, there was anomalous inflow upshear or left of tilt, and there was anomalous outflow downshear or right of tilt (Fig. 5a). Additionally, the background, storm-relative flow was north-northwesterly (not shown), projecting onto radial flow anomalies at >300-km radius. Anomalies in θ_e mimicked the pattern in radial flow anomalies, with relatively low-θ_e upshear or left of tilt and relatively high θ_e downshear or right of tilt (Fig. 5b). As a result of this positive spatial correlation between u' and θ_e', $u'\theta_e'$ was predominately positive, with the largest values (20–25 m s^{-1} K) upshear or left of tilt (Fig. 5c). The upshear ventilation signature, where $u' < 0$ and $\theta_e' < 0$, coincided with the dry-air intrusion seen in Fig. 2b. When azimuthally averaged, the positive $u'\theta_e'$ would have contributed to a decrease in θ_e in and around the inner core due to an eddy flux divergence between the center and the radius of the inner circumnavigation.

Similar wavenumber-1 asymmetries in u' and θ_e' were seen in the middle layer (Figs. 5d,e). The background, storm-relative flow was north-northeasterly (not shown) and was consistent with the radial flow anomalies at >300-km radius. The largest radial ventilation was in the downtilt-left quadrant or left of shear (Fig. 5f). This spiraling inward structure of the radial ventilation was reminiscent of the 5-km altitude radial ventilation structure seen in the idealized simulations of Alland et al. (2021b) (see their Fig. 4). Additionally, anomalous outward

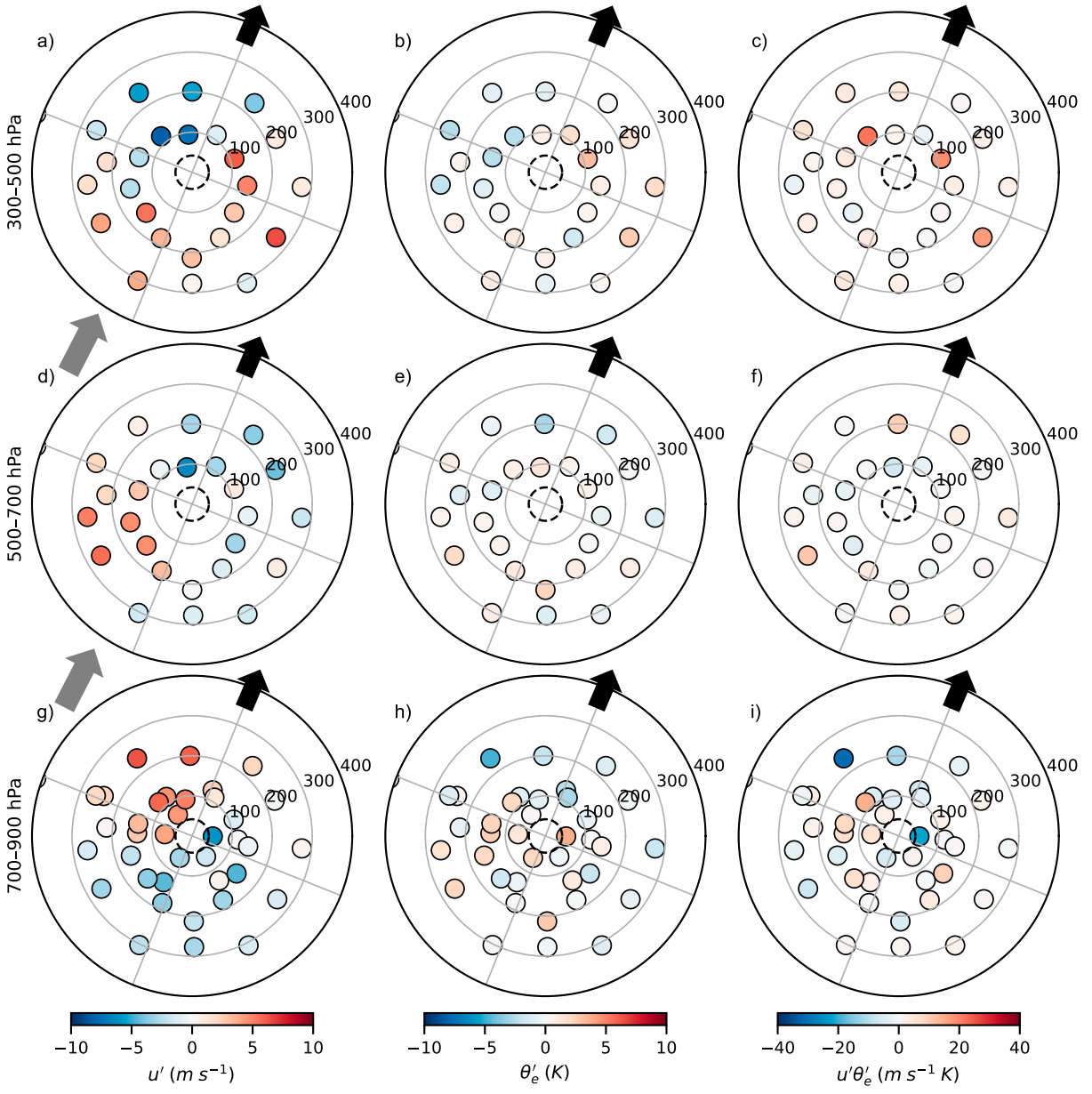

FIG. 4. Radial ventilation analysis for the first sampling period around 0000 UTC 26 Sep 2021: (a) anomalous storm-relative radial wind (m s^{-1}), (b) anomalous θ_e (K), and (c) $u'\theta'_e$ (m s^{-1} K) averaged over the 300–500-hPa layer. (d)–(f) As in (a)–(c), but averaged over 500–700 hPa. (g)–(i) As in (a)–(c), but averaged 700–900 hPa. The black arrow shows the 1–6.5-km tilt direction with tilt-relative quadrants demarcated. Range rings are every 100 km, and the dashed, black circle indicates 1.5 times the radius of maximum wind. The gray arrow indicates the shear direction.

fluxes of the relatively high-θ_e air occurred in the uptilt-right quadrant. While this signal is not ventilation per se, other studies have noted this signature in sheared TCs and hypothesized it could be relevant for intensity change (Gu et al. 2015; Riemer and Laliberté 2015).

In the lower layer, there was anomalous inflow downshear or right of tilt and anomalous outflow upshear or left of tilt (Fig. 5g), opposite of that in the upper layer, which is consistent with other observational composites of TCs in shear (DeHart et al. 2014; Boehm and Bell 2021). Anomalies in θ_e were less coherent, but there was a tendency for positive perturbations to cluster in the uptilt-right quadrant and negative perturbations to cluster in the downtilt semicircle between 100 and 300 km (Fig. 5h). From a shear-relative perspective, the location of these θ_e anomalies was consistent with the dropsonde composite analyses of Zhang et al. (2013) and Nguyen et al. (2019). The overlap between the region of anomalous inflow and negative θ_e anomalies resulted in radial

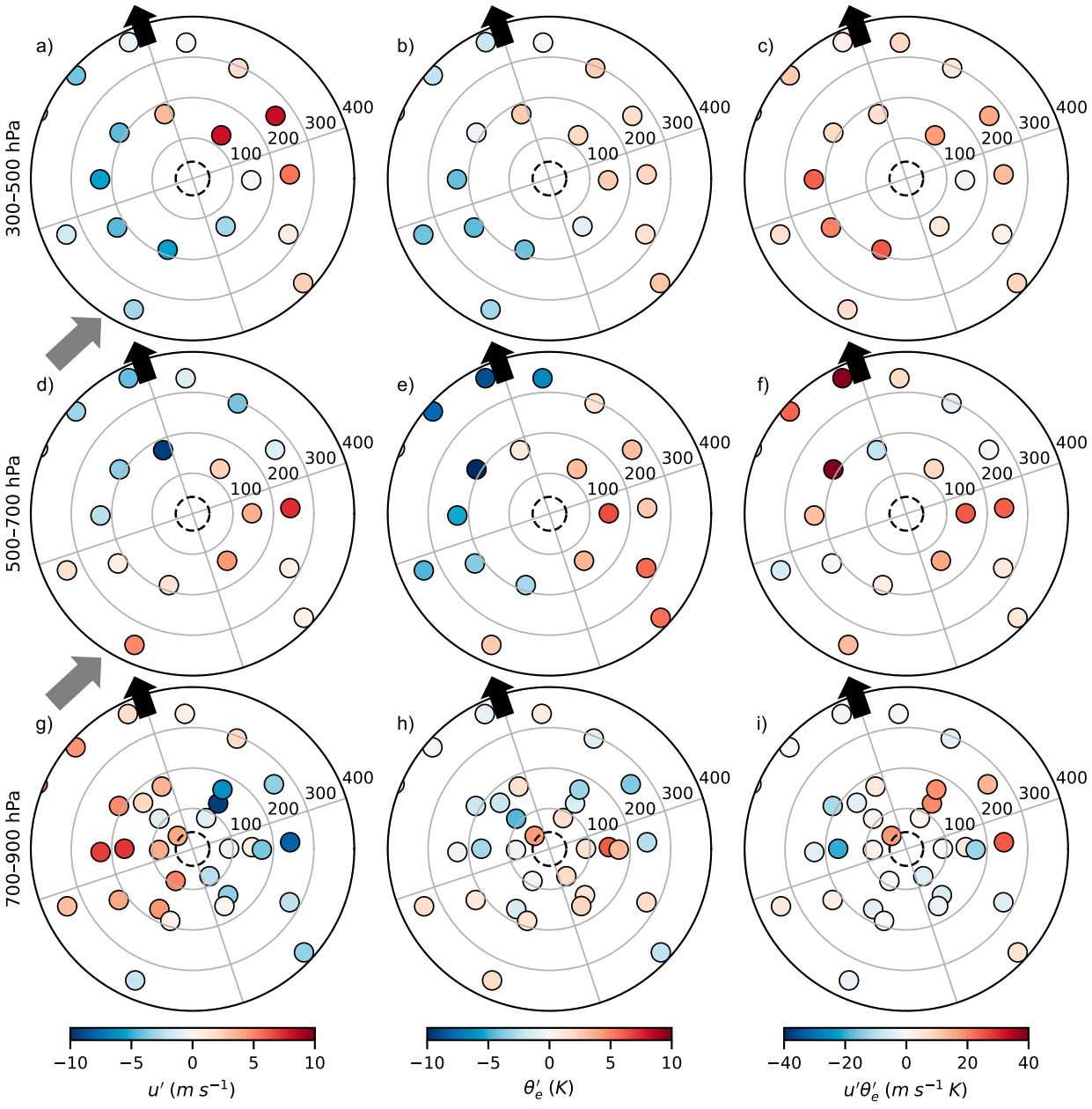

FIG. 5. As in Fig. 4, but for the second sampling period around 0000 UTC 27 Sep 2021.

ventilation in the downtilt-right quadrant (Fig. 5i), consistent with the location of radial ventilation outside 100-km radius in Alland et al. (2021b). The combined, stronger ventilation signatures, particularly downtilt right in the lower layer and left of tilt in the middle and upper layers, were consistent with ventilation-induced weakening of Sam.

Figure 6 shows the ventilation analysis for the third sampling period around the start of reintensification. In contrast to the second sampling period, the wavenumber-1 patterns in u' and θ'_e in the upper and middle layers within 250-km radius have rotated counterclockwise (Figs. 6a,b,d,e), following the counterclockwise rotation of the tilt. While there was still a coherent area of radial ventilation to the south of the center in the upper layer, the overall radial ventilation signal was diminished in both the upper and middle layers (Figs. 6c,f). In the lower layer, the downtilt-right ventilation signal weakened. The diminished radial ventilation in all layers was consistent with the subsequent reintensification of Sam.

b. *Vertical structure*

We only focused on the second sampling period, when the radial ventilation was relatively large. We grouped dropsondes within 100–300-km radius by tilt-relative quadrants to explore thermodynamic and radial ventilation structure differences

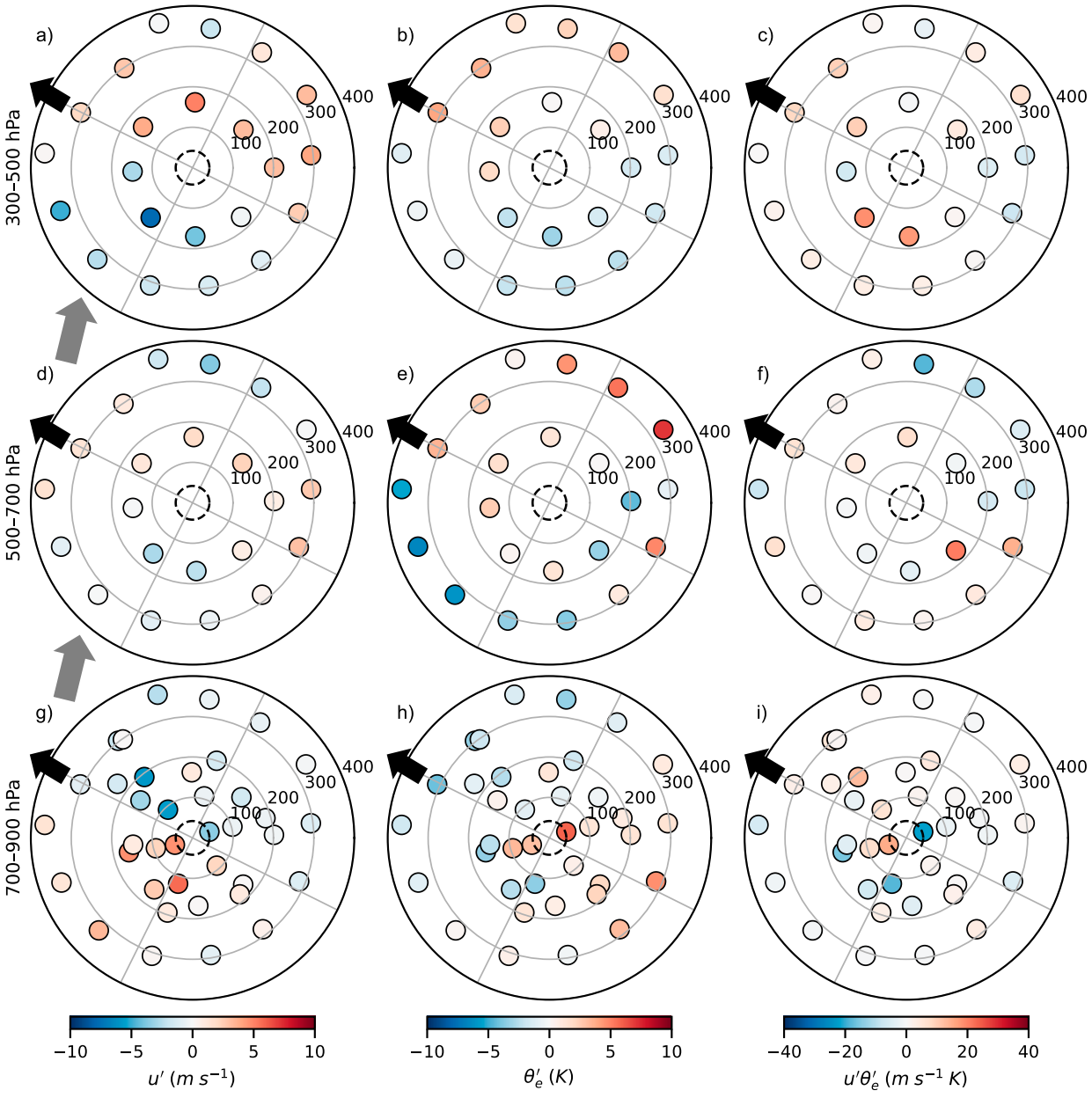

FIG. 6. As in Fig. 4, but for the third sampling period around 0000 UTC 28 Sep 2021.

between quadrants. Since the number of dropsondes per quadrant was small, particularly ones that sampled the deep troposphere, we did not assess whether differences between quadrants were statistically significant. Instead, we looked for vertically coherent radial ventilation layers, where $u' < 0$ and $\theta_e' < 0$, and where there was some consistency between dropsondes.

Figures 7a and 7c show dry layers in the mid- to upper troposphere in the left-of-tilt quadrants. Associated with these dry layers were negative perturbations in θ_e (Figs. 8a,c). Additionally, $u' < 0$ in the mid- to upper troposphere, resulting in a coherent layer of radial ventilation with a mean around 15–25 m s^{-1} K between 300 and 600 hPa.

Large differences existed between individual dropsonde profiles in the downtilt-left quadrant (Figs. 7a and 8a). These large differences were attributed to dropsondes sampling both the relatively moist, high-θ_e air ascending in rainbands and the relatively dry, low-θ_e air radially outward of rainbands. One profile about 200 km northwest of the center had radial ventilation values approaching 75 m s^{-1} K (see the rightmost gray line in Fig. 8a), indicating potential for rainbands to be ventilated and downdrafts to be produced via evaporation and sublimation. A caveat is that it is unknown how much farther inward this radial ventilation extended.

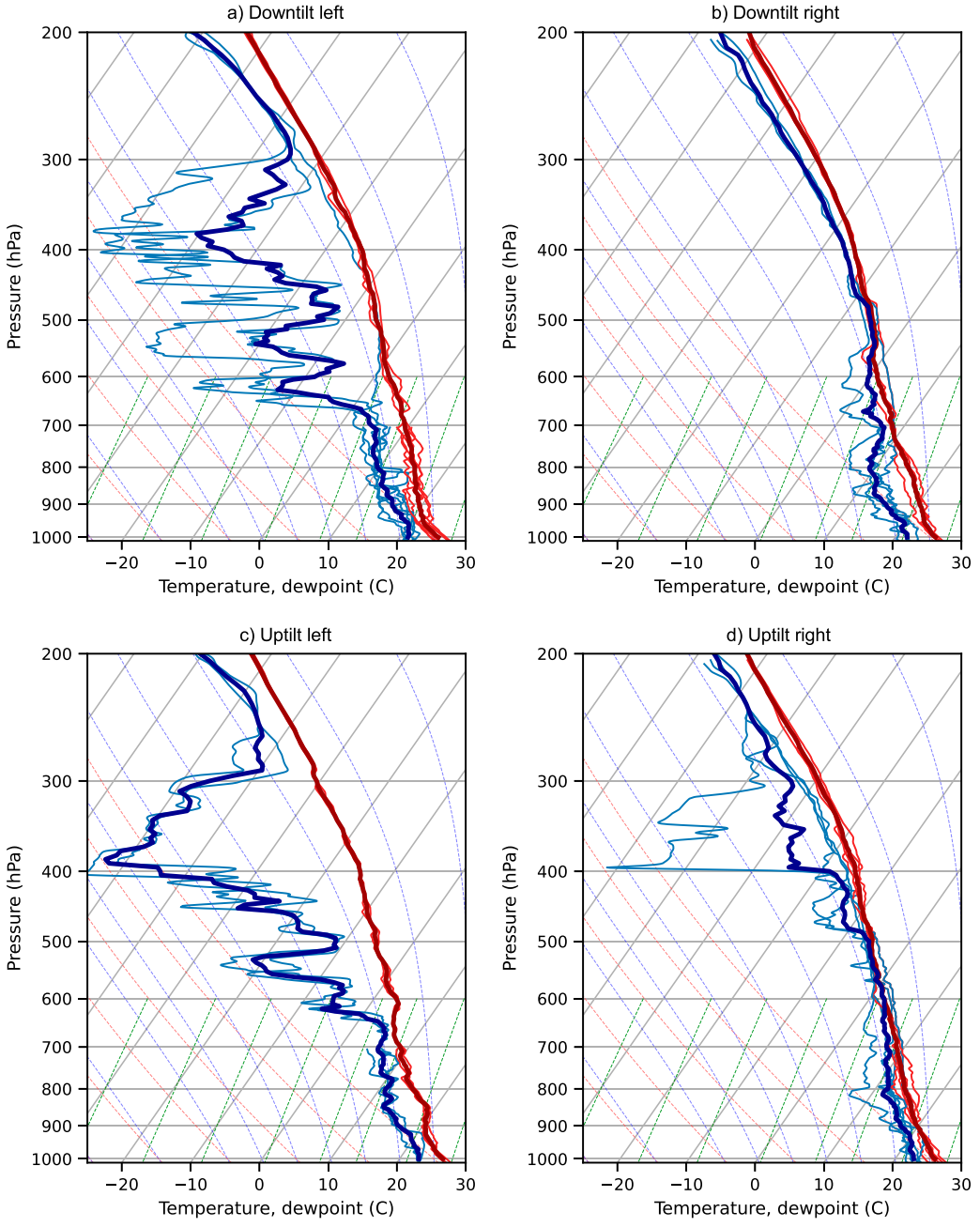

FIG. 7. Skew T–log$p$ diagrams of the temperature (red lines) and dewpoint (blue lines) for the (a) downtilt-left, (b) downtilt-right, (c) uptilt-left, and (d) uptilt-right quadrants. The mean profile within each quadrant is given by the darker, thicker lines, and the individual dropsonde profiles are given by the lighter, thinner lines.

In contrast to the left-of-tilt quadrants, the right-of-tilt quadrants had profiles that were more moist (Figs. 7b,d). In the downtilt-right quadrant, the profile was nearly saturated and moist adiabatic in the mid- to upper troposphere. Between 750 and 950 hPa, the thermodynamic profile had hints of an onion-type structure, which is associated with mesoscale downdrafts (Zipser 1977). Within this layer, there were negative perturbations in θ_e (Fig. 8b). Storm-relative radial inflow also existed below 700 hPa, resulting in a coherent layer of radial ventilation with a mean around 10–20 m s^{-1} K between 750 and 900 hPa, although a few profiles had radial ventilation >25 m s^{-1} K. The uptilt-right quadrant did not have any consistent, coherent layers of radial ventilation (Fig. 8d). Between 500 and 700 hPa, however, positive perturbations of u' and θ_e' resulted in a positive eddy flux in this layer, consistent with what was observed in Fig. 5f.

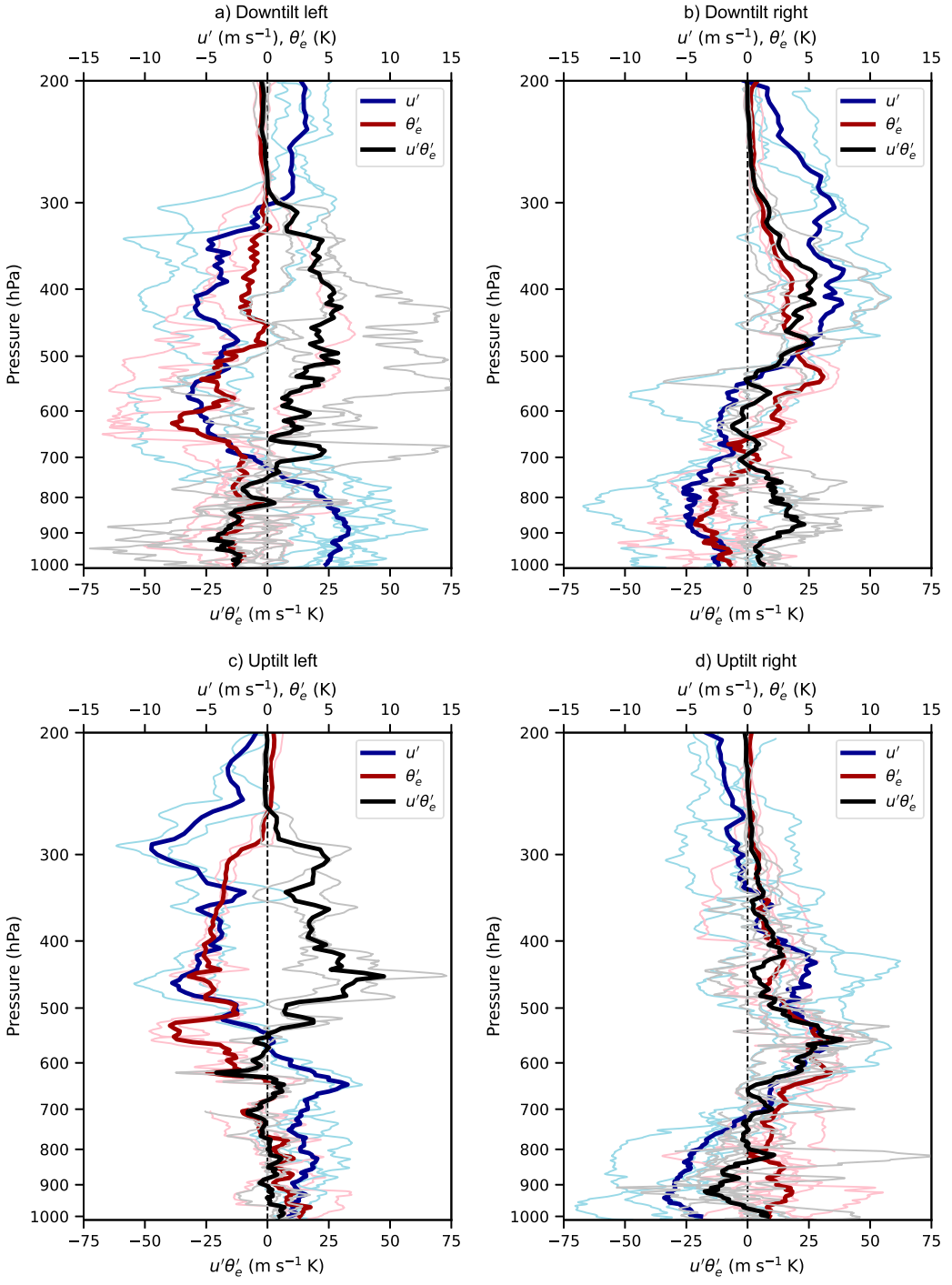

FIG. 8. Profiles of the anomalous storm-relative radial wind (m s^{-1}; blue lines), anomalous θ_e (K; red lines), and $u'\theta'_e$ (m s^{-1} K; black lines) for the (a) downtilt-left, (b) downtilt-right, (c) uptilt-left, and (d) uptilt-right quadrants. The mean profile within each quadrant is given by the darker, thicker lines, and the individual dropsonde profiles are given by the lighter, thinner lines.

We summarize a couple of key points based on this analysis. First, it is difficult to deduce radial ventilation from the skew T–log$p$ profiles alone. Dry, low-θ_e layers are clearly evident left of tilt but require coinciding anomalous inward flow to ventilate the TC. Dewpoint depressions need not be as large in the lower troposphere, such as in the downtilt-right quadrant, to achieve substantial θ_e deficits. Second, there is interquadrant variability in both the height and depth in which

radial ventilation occurs. The radial ventilation in Hurricane Sam during this period was focused between 300 and 600 hPa in the left-of-tilt quadrants and 750–900 hPa in the downtilt-right quadrant, suggesting distinct radial ventilation pathways related to different aspects of the TC structure (Alland et al. 2021b).

c. *Relationship to TC structure*

We used the Tropical Cyclone Radar Archive of Doppler Analyses with Recentering (TC-RADAR; Fischer et al. 2022) merged analyses from the P-3 tail Doppler radar to explore the link between the observed ventilation patterns in Sam with the tilt evolution and the stationary band complex. The horizontal resolution of the TC center data, used to calculate the tilt, is 2 km.

1) TILT EVOLUTION AND UPPER-LAYER VENTILATION

The tilt was diagnosed through TC-RADAR estimates of the vortex center location at various heights, as shown in Fig. 9, for the three P-3 missions of interest into Sam. During the first mission, the tilt was relatively small and in the same direction as the shear (Fig. 4). The tilt direction was consistent with the asymmetries in the radial flow seen in Fig. 4a—a tilt toward the northeast induced a radial flow component from the northwest (left of tilt) to the southeast (right of tilt) at upper levels.

Between the first and second P-3 mission, the tilt direction precessed cyclonically and increased in magnitude. For example, the 1–3-km tilt increased from 4 to about 9 km, and the 1–10-km tilt increased from 7 to 14 km. This increase in tilt was consistent with the increase in shear. The tilt during the second period pointed toward the north-northwest or in the downshear-left direction, a common tilt orientation relative to the shear vector (Jones 1995; Reasor et al. 2004, 2013; Reasor and Montgomery 2015; Fischer et al. 2022; Yu et al. 2023b). As a result, the radial wind anomaly dipole in the upper layer was oriented from the southwest to northeast (Fig. 5a), and large ventilation resulted from the combination of the anomalous radial inflow and the low-θ_e, dry-air intrusion on the western side of the TC (Figs. 5b,c).

Between the second and third P-3 mission, the tilt magnitude decreased and the tilt direction continued to precess cyclonically, particularly below 8-km height. This progress toward realignment and continued precession was consistent with the decrease in shear/ventilation and reestablishment of more symmetric deep convection around the center, leading to reintensification (Tao and Zhang 2016; Rios-Berrios et al. 2018; Chen et al. 2019; Alvey et al. 2020; Schecter and Menelaou 2020). Upper-layer radial wind anomalies were likewise consistent with the tilt direction (Fig. 6a), resulting in some continued ventilation to the south of the center (Fig. 6c).

What role did the background, storm-relative flow, versus the tilt, play in radial ventilation? Given Hurricane Sam was intense, and the storm-relative flow was weak (not shown), the tilt-induced radial wind anomalies likely dominated within 200–300 km of the center. Outward of 300-km radius, the storm-relative flow could have been more influential where

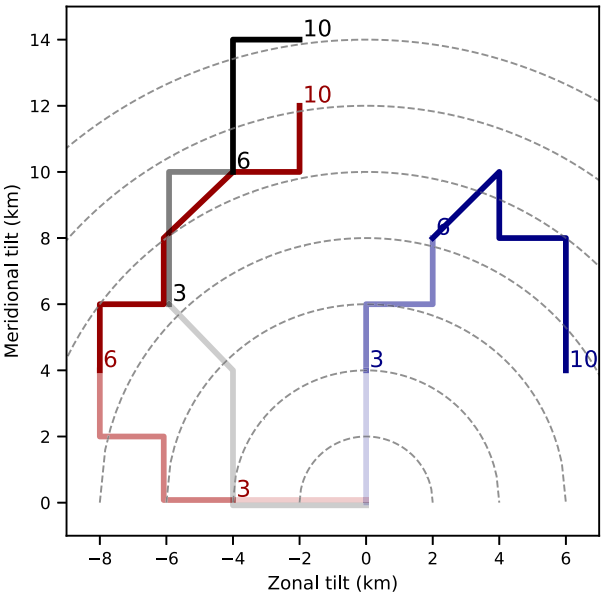

FIG. 9. Tilt hodographs derived from the merged TC-RADAR data for the P-3 missions for the first (blue), second (black), and third (red) sampling periods. Tilts are relative to the 1-km center at the origin, where the hodograph begins. The portion of the tilt hodograph from 1 to 3 km is in the lightest shading, 3–6 km in the medium shading, and 6–10 km in the darkest shading. Specific levels (3, 6, and 10 km) are annotated. Range rings are every 2 km.

the TC flow was weaker, consistent with simple kinematic models of environmental flow interacting with TCs (Riemer and Montgomery 2011). The main role of the background, shear flow was to force the TC tilt, rather than directly ventilate the TC.

In summary, the tilt evolution in Sam, induced by the shear changes, seemed to have played an important role in allowing for the transient period of upper-layer ventilation. The ventilation was maximized when the radial flow anomalies predominately induced by the tilt became spatially correlated with the θ_e anomalies. This correlation implied a more effective transport of low-θ_e air inward, which could negatively affect convection. Although that effect is hard to discern with these dropsonde observations alone. From a system-scale perspective, the period of greater azimuthally averaged $u'\theta_e' > 0$ would be consistent with a reduction in the inner-core θ_e, especially in the middle and upper layers.

2) STATIONARY BAND COMPLEX AND LOWER-LAYER VENTILATION

The shear-induced tilt also organizes the stationary band complex (Riemer 2016). The stratiform region of the stationary band complex is characterized by mid- to low-level mesoscale inflow (Didlake and Houze 2013), which is hypothesized to be the mesoscale feature responsible for lower-layer ventilation downshear and left of shear (Alland et al. 2021a). We now investigate the relationship between the inflow associated with the stationary band complex and lower-layer ventilation diagnosed during the second sampling period.

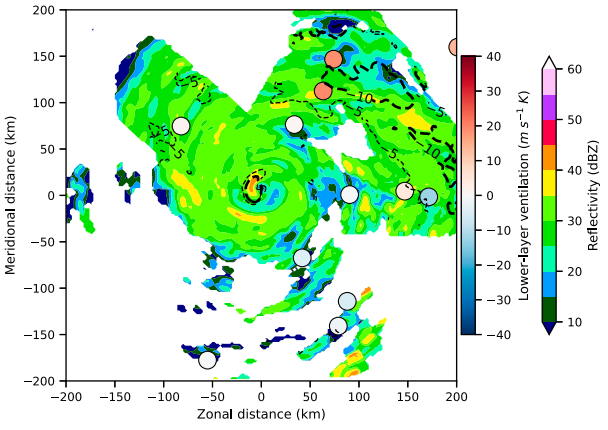

FIG. 10. Radar reflectivity (shaded) and storm-relative radial inflow (contoured at -5 and -10 m s^{-1}), averaged between 1- and 3-km height, from the merged TC-RADAR data for the second sampling period. Overlaid circles show the lower-layer ventilation diagnosed from dropsonde observations, only shown where there is storm-relative radial inflow in the dropsonde data.

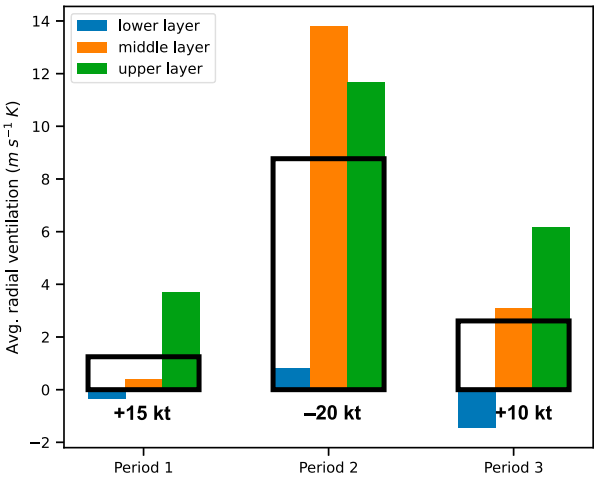

FIG. 11. The ventilation metric for the three sampling periods in Sam. The black bars show the ventilation metric averaged over 300–900 hPa; and the blue, orange, and green bars show the ventilation metric averaged over 700–900, 500–700, and 300–500 hPa. The 12-h intensity change from 1800 to 0600 UTC surrounding each observation period is also indicated.

Figure 10 shows the stationary band complex spiraled in from the eastern side of the storm toward the northwest side, consisting of a primary rainband and secondary rainbands, connecting with the inner-core precipitation. Along and outward of the spine of the stationary band complex was an area of radar-derived, storm-relative radial inflow that matched the area of the anomalous lower-layer inflow diagnosed in the dropsonde observations, particularly northeast of the center (Fig. 5g). The θ_e was anomalously low within this same area (Fig. 5h), presumably due to lower θ_e air being transported into this layer due to evaporative cooling. As a result, lower-layer ventilation was apparent within this part of the stationary band complex. This lower-layer ventilation pathway could possibly be detrimental to the intensity, although θ_e recovery may occur through surface enthalpy fluxes upon low-θ_e air reaching the boundary layer (Zhang et al. 2013; Alland and Davis 2022).

5. Ventilation metric

Given the potential operational utility of diagnosing ventilation, we suggest a scalar ventilation metric to measure the overall radial ventilation strength. The metric is the mass-weighted, volume average of $u'\theta_e'$ from 300 to 900 hPa and between 100- and 250-km radius. This metric is based off the original definition of ventilation in Tang and Emanuel (2010), which is the mass-weighted surface integral of the radial eddy flux of moist entropy. The chosen radial region is motivated by practical considerations, specifically to encompass the full-tropospheric sampling along the innermost G-IV circumnavigation.

In calculating this ventilation metric in practice, there are a couple of additional considerations. To include low-level P-3 observations and examine ventilation in specific layers, the vertical integral may be split into layers, such as the 700–900-, 500–700-, and 300–500-hPa layers that we have used herein. Then, a step should be taken to reduce biases in the azimuthal averaging caused by spatial sampling inhomogeneities. For example, a simple method is to bin and average values by quadrant. Then, the quadrant-averaged values may themselves be averaged together to estimate the horizontal average in each layer, as we have done here.

Figure 11 shows the ventilation metric for the three sampling periods. The overall ventilation strength was consistent with the intensity changes: relatively small ventilation during the rapid intensification period, relatively large ventilation during the rapid weakening period, and reduction of the ventilation at the start of reintensification. The individual-layer averages show that the radial ventilation was largest in mid- to upper levels of the troposphere, consistent with what is seen in Fig. 5, and the subsequent reduction in ventilation was driven by mid- to upper-level reductions seen in Fig. 6. Such summary ventilation statistics, which can be calculated in near–real time upon the completion of a mission, may give forecasters clues of ventilation-induced intensity changes that may be occurring or about to occur. The spatial structure of ventilation, however, should be considered, as there may be locally large ventilation that is not captured in the averaged metric, such as radial ventilation associated with the stationary band complex in the lower layer (Fig. 10).

6. Conclusions

This study offers a method to diagnose radial ventilation using dropsonde observations in TCs. The requirement is measurements of storm-relative radial wind and θ_e in some reasonably confined annulus around the storm center. Provided such a requirement is met, the storm-relative radial eddy flux of θ_e may be calculated to estimate the radial ventilation at the dropsonde observation locations. It is preferable to have dropsonde sampling over as deep of a layer as possible, such

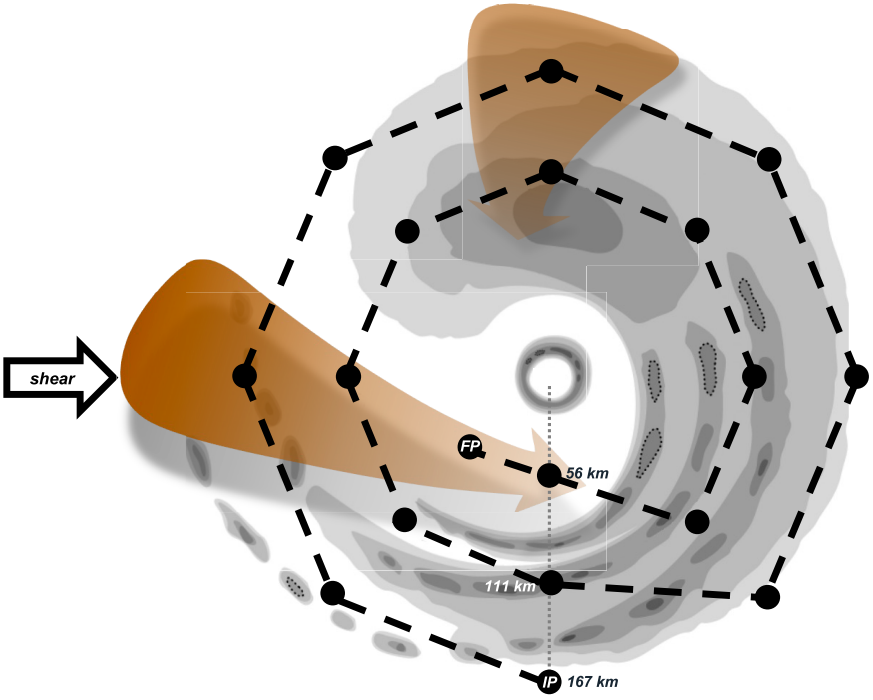

FIG. 12. Proposed G-IV flight pattern from the ventilation module, consisting of a double circumnavigation with an extra leg to sample the upshear ventilation pathway. Dropsonde release points are given by the circles, with the initial point (IP) and final point (FP) indicated. Conceptual radial ventilation pathways are indicated by the brown regions. Background image of the tropical cyclone structure in shear adapted from Hence and Houze (2012).

as with the high-altitude G-IV circumnavigation pattern in the outer-core or near-environment region of a TC.

Hurricane Sam offered an excellent case to evaluate radial ventilation changes due to the three consecutive days of sampling by both G-IV and P-3 aircraft. Over these 3 days, Sam underwent substantial fluctuations in structure and intensity—rapidly intensifying, rapidly weakening, and then slowly reintensifying.

During the first sampling period, there was little radial ventilation in Sam, despite there being some small vortex tilt toward the northwest. Even though this tilt induced some asymmetry in the storm-relative radial flow, there was little asymmetry in θ_e to produce radial ventilation of significance.

In contrast, the second sampling period featured a much larger radial ventilation, particularly between 700 and 300 hPa. As the shear increased in magnitude, due to the approach of an upper-level trough, the tilt increased. Simultaneously, low-θ_e, dry air wrapped in on the left-of-tilt (upshear) side of the storm. The correlation of the area of storm-relative radial inflow and anomalously low-θ_e air resulted in large radial ventilation at mid- to upper levels. Additionally, in the stationary band complex on the downtilt-right (downshear) side of the TC, there was evidence of mesoscale inflow of low-θ_e air at low- to midlevels. The location of these radial ventilation pathways, along with their effect on modulating Sam's intensity, is consistent with idealized and real-case modeling studies (e.g., Alland et al. 2021b; Fischer et al. 2023).

The third sampling period was characterized by a reduction in the ventilation, as the shear abated and as the tilt decreased and precessed upshear. The asymmetries in the storm-relative radial flow and θ_e were less correlated and generally not as large in magnitude, resulting in less radial ventilation.

It is important to keep in mind that ventilation variability is not the only cause of intensity changes in TCs. As mentioned previously, Sam underwent an eyewall replacement cycle around the same time that the ventilation increased. How both factors might have interacted to result in the rapid weakening and subsequent reintensification is a complicated question that we do not address here, but it raises intriguing questions about how eyewall replacement cycles and intensity respond to ventilation during different TC stages (Finocchio and Rios-Berrios 2021; Yu et al. 2021).

Additionally, while radial ventilation was clearly present around Sam between 125- and 250-km radius, radial ventilation pathways inward of 125 km and above 700 hPa were less evident due to fewer observations. To address this issue, one possibility is to design specific flight pattern modules, or perform targeted observations (Torn 2014), that would sample this region. Motivated by the analysis of Hurricane Sam, we proposed a ventilation module for the NOAA Hurricane Field Program (HFP) for mature-stage TCs. Figure 12 shows the proposed G-IV circumnavigation pattern for the ventilation module in the 2024 HFP, which includes a tighter circumnavigation and an extra leg to sample inward of 125 km when

safety allows. This module would build upon G-IV sampling strategies that benefit both research and operations (Sippel et al. 2024). Another possibility is to examine ventilation in the numerical weather prediction model output, particularly high-resolution TC models that assimilate the aircraft observations. Observations of other fields may also reveal the effects of ventilation, such as a weakening of convection and presence of downdrafts. The weakening of convection may also be brought about by subsidence and warming on the uptilt side associated with the dynamical response to increasing tilt. In addition to radial ventilation, downdraft ventilation is an important ventilation pathway that may also be examined with dropsondes and aircraft Doppler radar, which we aim to do in follow-on work. The scope here was to provide a way to diagnose radial ventilation with dropsonde observations.

A radial ventilation analysis over a larger sample of cases, particularly cases with G-IV circumnavigation patterns, would establish if there is consistency in radial ventilation locations and vertical structure and evaluate the degree of statistical relationship between the ventilation metric and intensity changes. When combined with TC-RADAR or other observations, a more comprehensive analysis would be promising for relating multiple aspects of the TC structure with ventilation pathways and effects.

Acknowledgments. This research was supported by the Office of Naval Research Grants N000142012071 and N000142312443 and National Science Foundation Grant AGS1748779. We thank three anonymous reviewers for their constructive comments.

Data availability statement. All datasets used in this study (ERA5, IR satellite, SHIPS output, dropsonde, and TC-RADAR data) are publicly available from their respective sources. Dropsonde data are from the NOAA/Atlantic Oceanographic and Meteorological Laboratory/Hurricane Research Division. The Atmospheric Sounding Processing Environment software is available from NCAR/EOL.

REFERENCES

Ahern, K., and L. Cowan, 2018: Minimizing common errors when projecting geospatial data onto a vortex-centered space. *Geophys. Res. Lett.*, **45**, 12 032–12 039, https://doi.org/10.1029/2018GL079953.

Alland, J. J., and C. A. Davis, 2022: Effects of surface fluxes on ventilation pathways and the intensification of Hurricane Michael (2018). *J. Atmos. Sci.*, **79**, 1211–1229, https://doi.org/10.1175/JAS-D-21-0166.1.

——, B. H. Tang, K. L. Corbosiero, and G. H. Bryan, 2021a: Combined effects of midlevel dry air and vertical wind shear on tropical cyclone development. Part I: Downdraft ventilation. *J. Atmos. Sci.*, **78**, 763–782, https://doi.org/10.1175/JAS-D-20-0054.1.

——, ——, ——, and ——, 2021b: Combined effects of midlevel dry air and vertical wind shear on tropical cyclone development. Part II: Radial ventilation. *J. Atmos. Sci.*, **78**, 783–796, https://doi.org/10.1175/JAS-D-20-0055.1.

Alvey, G. R., III, E. Zipser, and J. Zawislak, 2020: How does Hurricane Edouard (2014) evolve toward symmetry before rapid intensification? A high-resolution ensemble study. *J. Atmos. Sci.*, **77**, 1329–1351, https://doi.org/10.1175/JAS-D-18-0355.1.

Boehm, A. M., and M. M. Bell, 2021: Retrieved thermodynamic structure of Hurricane Rita (2005) from airborne multi–Doppler radar data. *J. Atmos. Sci.*, **78**, 1583–1605, https://doi.org/10.1175/JAS-D-20-0195.1.

Chavas, D. R., 2017: A simple derivation of tropical cyclone ventilation theory and its application to capped surface entropy fluxes. *J. Atmos. Sci.*, **74**, 2989–2996, https://doi.org/10.1175/JAS-D-17-0061.1.

Chen, X., J. A. Zhang, and F. D. Marks, 2019: A thermodynamic pathway leading to rapid intensification of tropical cyclones in shear. *Geophys. Res. Lett.*, **46**, 9241–9251, https://doi.org/10.1029/2019GL083667.

Corbosiero, K. L., and J. Molinari, 2002: The effects of vertical wind shear on the distribution of convection in tropical cyclones. *Mon. Wea. Rev.*, **130**, 2110–2123, https://doi.org/10.1175/1520-0493(2002)130<2110:TEOVWS>2.0.CO;2.

Cram, T. A., J. Persing, M. T. Montgomery, and S. A. Braun, 2007: A Lagrangian trajectory view on transport and mixing processes between the eye, eyewall, and environment using a high-resolution simulation of Hurricane Bonnie (1998). *J. Atmos. Sci.*, **64**, 1835–1856, https://doi.org/10.1175/JAS3921.1.

Davis, C. A., and D. A. Ahijevych, 2012: Mesoscale structural evolution of three tropical weather systems observed during PREDICT. *J. Atmos. Sci.*, **69**, 1284–1305, https://doi.org/10.1175/JAS-D-11-0225.1.

DeHart, J. C., R. A. Houze Jr., and R. F. Rogers, 2014: Quadrant distribution of tropical cyclone inner-core kinematics in relation to environmental shear. *J. Atmos. Sci.*, **71**, 2713–2732, https://doi.org/10.1175/JAS-D-13-0298.1.

Didlake, A. C., Jr., and R. A. Houze Jr., 2013: Dynamics of the stratiform sector of a tropical cyclone rainband. *J. Atmos. Sci.*, **70**, 1891–1911, https://doi.org/10.1175/JAS-D-12-0245.1.

Emanuel, K., C. DesAutels, C. Holloway, and R. Korty, 2004: Environmental control of tropical cyclone intensity. *J. Atmos. Sci.*, **61**, 843–858, https://doi.org/10.1175/1520-0469(2004)061<0843:ECOTCI>2.0.CO;2.

Euler, C., M. Riemer, T. Kremer, and E. Schömer, 2019: Lagrangian description of air masses associated with latent heat release in Tropical Storm Karl (2016) during extratropical transition. *Mon. Wea. Rev.*, **147**, 2657–2676, https://doi.org/10.1175/MWR-D-18-0422.1.

Finocchio, P. M., and R. Rios-Berrios, 2021: The intensity- and size-dependent response of tropical cyclones to increasing vertical wind shear. *J. Atmos. Sci.*, **78**, 3673–3690, https://doi.org/10.1175/JAS-D-21-0126.1.

Fischer, M. S., P. D. Reasor, R. F. Rogers, and J. F. Gamache, 2022: An analysis of tropical cyclone vortex and convective characteristics in relation to storm intensity using a novel airborne Doppler radar database. *Mon. Wea. Rev.*, **150**, 2255–2278, https://doi.org/10.1175/MWR-D-21-0223.1.

——, ——, B. H. Tang, K. L. Corbosiero, R. D. Torn, and X. Chen, 2023: A tale of two vortex evolutions: Using a high-resolution ensemble to assess the impacts of ventilation on a tropical cyclone rapid intensification event. *Mon. Wea. Rev.*, **151**, 297–320, https://doi.org/10.1175/MWR-D-22-0037.1.

Fu, H., Y. Wang, M. Riemer, and Q. Li, 2019: Effect of unidirectional vertical wind shear on tropical cyclone intensity change—Lower-layer shear versus upper-layer shear. *J. Geophys. Res. Atmos.*, **124**, 6265–6282, https://doi.org/10.1029/2019JD030586.

Gu, J.-F., Z.-M. Tan, and X. Qiu, 2015: Effects of vertical wind shear on inner-core thermodynamics of an idealized simulated tropical cyclone. *J. Atmos. Sci.*, **72**, 511–530, https://doi.org/10.1175/JAS-D-14-0050.1.

Hence, D. A., and R. A. Houze Jr., 2012: Vertical structure of tropical cyclone rainbands as seen by the TRMM precipitation radar. *J. Atmos. Sci.*, **69**, 2644–2661, https://doi.org/10.1175/JAS-D-11-0323.1.

Hersbach, H., and Coauthors, 2020: The ERA5 global reanalysis. *Quart. J. Roy. Meteor. Soc.*, **146**, 1999–2049, https://doi.org/10.1002/qj.3803.

Hoogewind, K. A., D. R. Chavas, B. A. Schenkel, and M. E. O'Neill, 2020: Exploring controls on tropical cyclone count through the geography of environmental favorability. *J. Climate*, **33**, 1725–1745, https://doi.org/10.1175/JCLI-D-18-0862.1.

Houze, R. A., Jr., 2010: Clouds in tropical cyclones. *Mon. Wea. Rev.*, **138**, 293–344, https://doi.org/10.1175/2009MWR2989.1.

Hsieh, T.-L., G. A. Vecchi, W. Yang, I. M. Held, and S. T. Garner, 2020: Large-scale control on the frequency of tropical cyclones and seeds: A consistent relationship across a hierarchy of global atmospheric models. *Climate Dyn.*, **55**, 3177–3196, https://doi.org/10.1007/s00382-020-05446-5.

Janowiak, J., B. Joyce, and P. Xie, 2017: NCEP/CPC L3 Half Hourly 4km Global (60S - 60N) Merged IR V1. Goddard Earth Sciences Data and Information Services Center, accessed 1 August 2023, https://doi.org/10.5067/P4HZB9N27EKU.

Jones, S. C., 1995: The evolution of vortices in vertical shear. I: Initially barotropic vortices. *Quart. J. Roy. Meteor. Soc.*, **121**, 821–851, https://doi.org/10.1002/qj.49712152406.

Leroux, M.-D., M. Plu, and F. Roux, 2016: On the sensitivity of tropical cyclone intensification under upper-level trough forcing. *Mon. Wea. Rev.*, **144**, 1179–1202, https://doi.org/10.1175/MWR-D-15-0224.1.

Lin, N., R. Jing, Y. Wang, E. Yonekura, J. Fan, and L. Xue, 2017: A statistical investigation of the dependence of tropical cyclone intensity change on the surrounding environment. *Mon. Wea. Rev.*, **145**, 2813–2831, https://doi.org/10.1175/MWR-D-16-0368.1.

Martin, C., and I. Suhr, 2021: Atmospheric Sounding Processing ENvironment (ASPEN) software (Version 3.4.9). NCAR/EOL, https://www.eol.ucar.edu/content/aspen.

Nguyen, L. T., R. Rogers, J. Zawislak, and J. A. Zhang, 2019: Assessing the influence of convective downdrafts and surface enthalpy fluxes on tropical cyclone intensity change in moderate vertical wind shear. *Mon. Wea. Rev.*, **147**, 3519–3534, https://doi.org/10.1175/MWR-D-18-0461.1.

Pasch, R. J., and D. P. Roberts, 2022: Tropical cyclone report: Hurricane Sam (AL182021), 22 September–5 October 2021. NHC Tech. Rep., 19 pp., https://www.nhc.noaa.gov/data/tcr/AL182021_Sam.pdf.

Peirano, C. M., K. L. Corbosiero, and B. H. Tang, 2016: Revisiting trough interactions and tropical cyclone intensity change. *Geophys. Res. Lett.*, **43**, 5509–5515, https://doi.org/10.1002/2016GL069040.

Powell, M. D., 1990: Boundary layer structure and dynamics in outer hurricane rainbands. Part II: Downdraft modification and mixed layer recovery. *Mon. Wea. Rev.*, **118**, 918–938, https://doi.org/10.1175/1520-0493(1990)118<0918:BLSADI>2.0.CO;2.

Reasor, P. D., and M. T. Montgomery, 2015: Evaluation of a heuristic model for tropical cyclone resilience. *J. Atmos. Sci.*, **72**, 1765–1782, https://doi.org/10.1175/JAS-D-14-0318.1.

——, ——, and L. D. Grasso, 2004: A new look at the problem of tropical cyclones in vertical shear flow: Vortex resiliency. *J. Atmos. Sci.*, **61**, 3–22, https://doi.org/10.1175/1520-0469(2004)061<0003:ANLATP>2.0.CO;2.

——, R. Rogers, and S. Lorsolo, 2013: Environmental flow impacts on tropical cyclone structure diagnosed from airborne Doppler radar composites. *Mon. Wea. Rev.*, **141**, 2949–2969, https://doi.org/10.1175/MWR-D-12-00334.1.

Richardson, J. C., R. D. Torn, and B. H. Tang, 2022: An analog comparison between rapidly and slowly intensifying tropical cyclones. *Mon. Wea. Rev.*, **150**, 2139–2156, https://doi.org/10.1175/MWR-D-21-0260.1.

Riemer, M., 2016: Meso-β-scale environment for the stationary band complex of vertically sheared tropical cyclones. *Quart. J. Roy. Meteor. Soc.*, **142**, 2442–2451, https://doi.org/10.1002/qj.2837.

——, and M. T. Montgomery, 2011: Simple kinematic models for the environmental interaction of tropical cyclones in vertical wind shear. *Atmos. Chem. Phys.*, **11**, 9395–9414, https://doi.org/10.5194/acp-11-9395-2011.

——, and F. Laliberté, 2015: Secondary circulation of tropical cyclones in vertical wind shear: Lagrangian diagnostic and pathways of environmental interaction. *J. Atmos. Sci.*, **72**, 3517–3536, https://doi.org/10.1175/JAS-D-14-0350.1.

——, M. T. Montgomery, and M. E. Nicholls, 2010: A new paradigm for intensity modification of tropical cyclones: Thermodynamic impact of vertical wind shear on the inflow layer. *Atmos. Chem. Phys.*, **10**, 3163–3188, https://doi.org/10.5194/acp-10-3163-2010.

——, ——, and ——, 2013: Further examination of the thermodynamic modification of the inflow layer of tropical cyclones by vertical wind shear. *Atmos. Chem. Phys.*, **13**, 327–346, https://doi.org/10.5194/acp-13-327-2013.

Rios-Berrios, R., and R. D. Torn, 2017: Climatological analysis of tropical cyclone intensity changes under moderate vertical wind shear. *Mon. Wea. Rev.*, **145**, 1717–1738, https://doi.org/10.1175/MWR-D-16-0350.1.

——, C. A. Davis, and R. D. Torn, 2018: A hypothesis for the intensification of tropical cyclones under moderate vertical wind shear. *J. Atmos. Sci.*, **75**, 4149–4173, https://doi.org/10.1175/JAS-D-18-0070.1.

Ryglicki, D. R., J. D. Doyle, D. Hodyss, J. H. Cossuth, Y. Jin, K. C. Viner, and J. M. Schmidt, 2019: The unexpected rapid intensification of tropical cyclones in moderate vertical wind shear. Part III: Outflow–environment interaction. *Mon. Wea. Rev.*, **147**, 2919–2940, https://doi.org/10.1175/MWR-D-18-0370.1.

Schecter, D. A., and K. Menelaou, 2020: Development of a misaligned tropical cyclone. *J. Atmos. Sci.*, **77**, 79–111, https://doi.org/10.1175/JAS-D-19-0074.1.

Shi, D., and G. Chen, 2023: Modulation of asymmetric inner-core convection on midlevel ventilation leading up to the rapid intensification of Typhoon Lekima (2019). *J. Geophys. Res. Atmos.*, **128**, e2022JD037952, https://doi.org/10.1029/2022JD037952.

Simpson, R. H., and H. Riehl, 1958: Mid-tropospheric ventilation as a constraint on hurricane development and maintenance. *Proc. Tech. Conf. on Hurricanes*, Miami Beach, FL, Amer. Meteor. Soc., D4-1–D4-10.

Sippel, J. A., S. D. Ditchek, K. Ryan, and C. W. Landsea, 2024: The G-IV inner circumnavigation: A story of successful organic interactions between research and operations at NOAA. *Bull. Amer. Meteor. Soc.*, **105**, E218–E232, https://doi.org/10.1175/BAMS-D-23-0084.1.

Tang, B., and K. Emanuel, 2010: Midlevel ventilation's constraint on tropical cyclone intensity. *J. Atmos. Sci.*, **67**, 1817–1830, https://doi.org/10.1175/2010JAS3318.1.

——, and ——, 2012a: A ventilation index for tropical cyclones. *Bull. Amer. Meteor. Soc.*, **93**, 1901–1912, https://doi.org/10.1175/BAMS-D-11-00165.1.

——, and ——, 2012b: Sensitivity of tropical cyclone intensity to ventilation in an axisymmetric model. *J. Atmos. Sci.*, **69**, 2394–2413, https://doi.org/10.1175/JAS-D-11-0232.1.

Tao, D., and F. Zhang, 2016: Effects of vertical wind shear on the predictability of tropical cyclones: Practical versus intrinsic limit. *J. Adv. Model. Earth Syst.*, **7**, 1534–1553, https://doi.org/10.1002/2015MS000474.

Torn, R. D., 2014: The impact of targeted dropwindsonde observations on tropical cyclone intensity forecasts of four weak systems during PREDICT. *Mon. Wea. Rev.*, **142**, 2860–2878, https://doi.org/10.1175/MWR-D-13-00284.1.

Wadler, J. B., D. S. Nolan, J. A. Zhang, and L. K. Shay, 2021: Thermodynamic characteristics of downdrafts in tropical cyclones as seen in idealized simulations of different intensities. *J. Atmos. Sci.*, **78**, 3503–3524, https://doi.org/10.1175/JAS-D-21-0006.1.

Weatherford, C. L., and W. M. Gray, 1988: Typhoon structure as revealed by aircraft reconnaissance. Part I: Data analysis and climatology. *Mon. Wea. Rev.*, **116**, 1032–1043, https://doi.org/10.1175/1520-0493(1988)116<1032:TSARBA>2.0.CO;2.

Wood, K. M., and E. A. Ritchie, 2015: A definition for rapid weakening of North Atlantic and eastern North Pacific tropical cyclones. *Geophys. Res. Lett.*, **42**, 10 091–10 097, https://doi.org/10.1002/2015GL066697.

Yu, C.-L., A. C. Didlake Jr., J. D. Kepert, and F. Zhang, 2021: Investigating axisymmetric and asymmetric signals of secondary eyewall formation using observations-based modeling of the tropical cyclone boundary layer. *J. Geophys. Res. Atmos.*, **126**, e2020JD034027, https://doi.org/10.1029/2020JD034027.

——, B. Tang, and R. G. Fovell, 2023a: Diverging behaviors of simulated tropical cyclones in moderate vertical wind shear. *J. Atmos. Sci.*, **80**, 2837–2860, https://doi.org/10.1175/JAS-D-23-0048.1.

——, ——, and ——, 2023b: Tropical cyclone tilt and precession in moderate shear: Precession hiatus in a critical shear regime. *J. Atmos. Sci.*, **80**, 909–932, https://doi.org/10.1175/JAS-D-22-0200.1.

Zawislak, J., H. Jiang, G. R. Alvey III, E. J. Zipser, R. F. Rogers, J. A. Zhang, and S. N. Stevenson, 2016: Observations of the structure and evolution of Hurricane Edouard (2014) during intensity change. Part I: Relationship between the thermodynamic structure and precipitation. *Mon. Wea. Rev.*, **144**, 3333–3354, https://doi.org/10.1175/MWR-D-16-0018.1.

Zhang, J. A., R. F. Rogers, P. D. Reasor, E. W. Uhlhorn, and F. D. Marks Jr., 2013: Asymmetric hurricane boundary layer structure from dropsonde composites in relation to the environmental vertical wind shear. *Mon. Wea. Rev.*, **141**, 3968–3984, https://doi.org/10.1175/MWR-D-12-00335.1.

Zipser, E. J., 1977: Mesoscale and convective–scale downdrafts as distinct components of squall-line structure. *Mon. Wea. Rev.*, **105**, 1568–1589, https://doi.org/10.1175/1520-0493(1977)105<1568:MACDAD>2.0.CO;2.